

## Examination of the Magneto-Structural Effects of Hangman Groups on Ferric Porphyrins by EPR

Joscha Nehr Korn,<sup>\*,†,‡,§</sup> Shannon A. Bonke,<sup>\*,†,§</sup> Azar Aliabadi,<sup>§</sup> Matthias Schwalbe,<sup>||</sup> and Alexander Schnegg<sup>†,§</sup>

<sup>†</sup>EPR Research Group, Max-Planck-Institut für Chemische Energiekonversion, Stiftstraße 34-36, 45470 Mülheim an der Ruhr, Germany

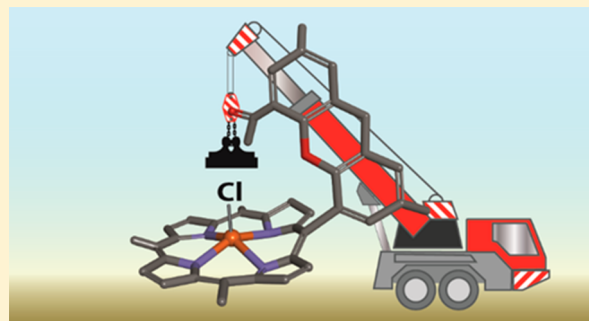
<sup>‡</sup>Institut für Anorganische und Angewandte Chemie, Universität Hamburg, Martin-Luther-King-Platz 6, 20146 Hamburg, Germany

<sup>§</sup>Institut Nanospektroskopie, Helmholtz-Zentrum Berlin für Materialien und Energie, Kekuléstraße 5, 12489 Berlin, Germany

<sup>||</sup>Institut für Chemie, Humboldt Universität zu Berlin, Brook-Taylor-Straße 2, 12489 Berlin, Germany

### Supporting Information

**ABSTRACT:** Ferric hangman porphyrins are bioinspired models for haem hydroperoxidase enzymes featuring an acid/base group in close vicinity to the metal center, which results in improved catalytic activity for reactions requiring O–O bond activation. These functional biomimics are examined herein with a combination of EPR techniques to determine the effects of the hanging group on the electronics of the ferric center. These results are compared to those for ferric octaethylporphyrin chloride [Fe(OEP)Cl], tetramesitylporphyrin chloride [Fe(TMP)Cl], and the pentafluorophenyl derivative [Fe(TPFPP)Cl], which were also examined herein to study the electronic effects of various substituents. Frequency-domain Fourier-transform THz-EPR combined with field domain EPR in a broad frequency range from 9.5 to 629 GHz allowed the determination of zero-field splitting parameters, revealing minor rhombicity  $E/D$  and  $D$  values in a narrow range of 6.24(8) to 6.85(5)  $\text{cm}^{-1}$ . Thus, the hangman porphyrins display  $D$  values in the expected range for ferric porphyrin chlorides, though  $D$  appears to be correlated with the Fe–Cl bond length. Extrapolating this trend to the ferric hangman porphyrin chlorides, for which no crystal structure has been reported, indicates a slightly elongated Fe–Cl bond length compared to the non-hangman equivalent.



## INTRODUCTION

Enzymatic catalysis typically utilizes a metal center (Lewis acid) to coordinate a substrate, with Brønsted acid–base groups often present to assist substrate positioning and orientation. Crucially, these groups abstract or supply protons for proton coupled electron transfer steps (PCET). The catalytic activity and selectivity of cytochrome *c* oxidase toward the PCET steps of the oxygen reduction reaction has led to it being coined “the mammalian fuel cell.”<sup>1</sup> Key to its catalytic activity are porphyrin structures of the haem structural family, and the importance of the reaction has inspired synthetic models. Biomimetic models aim to resemble the active site not only by the similar redox potential of the metal center but also by proximal sites for proton delivery/abstraction. These are essential for small molecule activation and PCET reactions, which are a foundation of efficient energy storage and utilization.<sup>1</sup>

Functional enzyme-inspired porphyrins have been synthesized with increasing sophistication and examined for catalytic activity toward a range of reactions (many requiring PCET steps). For example, planar ferric porphyrins have been reported as being active and selective catalysts for the

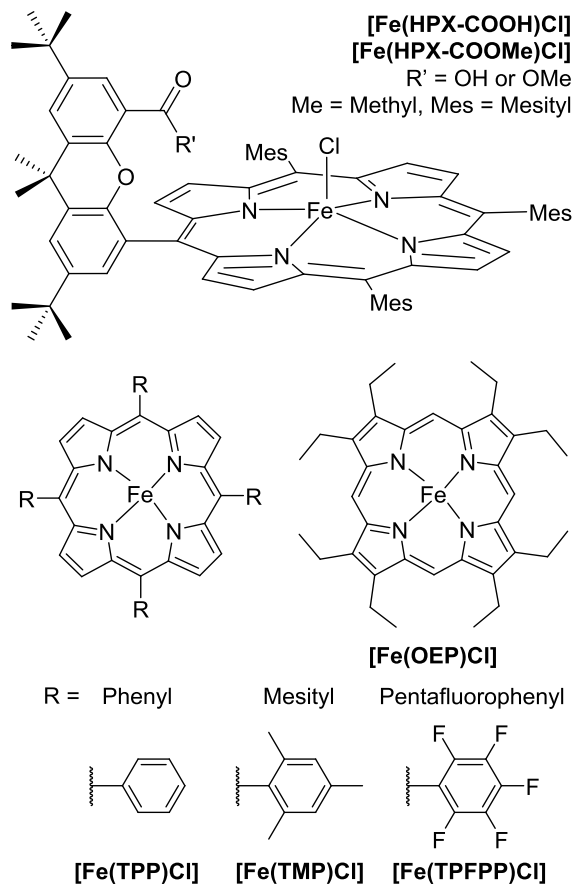
reduction of  $\text{CO}_2$  to CO and also allow the reduction of  $\text{CO}_2$  to  $\text{CH}_4$ .<sup>2</sup> Biomimetic models have evolved from planar porphyrin macrocycles to bimetallic systems<sup>3,4</sup> and cofacial biporphyrins such as the Pacman class of structures.<sup>5</sup> The latter is aptly named as it features two porphyrin units that are anchored by a single rigid pillar, which enables a small substrate molecule to move between the two porphyrin planes,<sup>5</sup> i.e., be eaten by the Pacman. The design envisions the substrate forming a dative bond to one or both metal centers, with electrostatic interaction with the second porphyrin making this substrate activation more favorable and stabilizing the process. First generation Pacman structures were diporphyrin anthracene (DPA) and diporphyrin biphenylene (DPB), referring to the linking pillar.<sup>1,5,6</sup> The rigid backbone of these structures results in near-parallel porphyrin units with limited flexibility. The linking pillars of second generation Pacman biporphyrins,<sup>1</sup> diporphyrin xanthene (DPX)<sup>7</sup> and diporphyrin dibenzofuran (DPD),<sup>8</sup> allowed greater flexibility in the angle between the two porphyrin units,

Received: August 2, 2019

allowing the Pacman to open and have greater interaction with substrate species.<sup>9</sup> This correlated with improved (photo)-catalytic activity toward certain oxidation reactions.<sup>9,10</sup>

The subsequently developed hangman structures aimed to provide a Brønsted acid–base group proximal to the porphyrin metal center, as is present in many enzymes. This was synthetically achieved by retaining the rigid pillar of a Pacman biporphyrin but replacing the second porphyrin with a carboxylic acid group that could hang above the center of a porphyrin (Scheme 1).<sup>11</sup> The Brønsted acid–base group

**Scheme 1. Structures of Ferric Porphyrins Spectroscopically Examined Herein<sup>a</sup>**



<sup>a</sup>Hangman architecture based on a mesityl-substituted porphyrin with chloride axial ligand, xanthene pillar, and hanging carboxylic acid [Fe(HPX-COOH)Cl] or methyl carboxylate [Fe(HPX-COOMe)Cl] (upper). Ferric tetra-arylporphyrins with phenyl, mesityl, or pentafluorophenyl substituents, with axial chloride ligand omitted, and ferric octaethylporphyrin (lower).

directly above the metal center is designed to orient the substrate above a catalytic active site to facilitate PCET. This is specifically interesting for small molecule activation, such as H<sub>2</sub>O<sub>2</sub> dismutation (catalase reaction) or O<sub>2</sub> activation.<sup>1,12</sup> For iron hangman porphyrins as well as corroles, it has been demonstrated that the carboxylic acid group had a positive influence on the catalytic activity.<sup>13–16</sup>

Catalytic activity is defined by the structural and electronic properties of a molecule or material. As such, determining these parameters with accuracy is crucial to rational catalyst development. For paramagnetic metalloporphyrins, such as hemes, the magnetic properties offer a spectroscopic handle to

better understand the species.<sup>17,18</sup> These magnetic properties are highly sensitive to the electronic structure and can subsequently be related back to chemical properties via magneto-structural correlations, which are rapidly improving in accuracy due to developments in theory and computational approaches.<sup>18–20</sup> This information is especially valuable for porphyrins that are hitherto unable to be crystallized such as the mesityl substituted hangman porphyrins with chloride axial ligands examined herein.

As in planar porphyrins, coordination of iron into a hangman structure often results in a 5-coordinate, square pyramidal geometry, combining the tetradentate porphyrin macrocycle and an additional ligand (e.g., Cl<sup>−</sup> or OH<sup>−</sup>). The metal center is displaced from the plane of the porphyrin, thus preventing other ligands from approaching the final (sixth) coordination site through repulsion by the delocalized negative charge of the conjugated porphyrin. If the hangman group is sterically bulky, the axial ligand may be more stable on the opposite side of the porphyrin plane—though this would diminish any catalytic benefits. Contrarily, hydrogen bonding between the hangman motif and the axial ligand has been demonstrated to result in them sharing the same porphyrin face in the case of a hangman porphyrin crystal structure with a hydroxide axial ligand and hanging carboxylic acid group.<sup>11</sup>

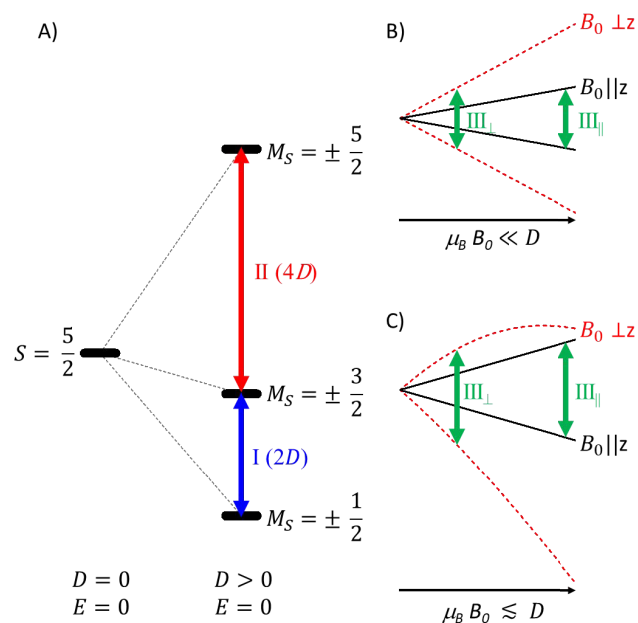
For paramagnetic systems with  $S \geq 1$ , a zero-field splitting (ZFS) can often be observed. ZFS arises from dipolar and spin–orbit couplings splitting otherwise degenerate spin states, and resulting in differences in spin state energy levels absent a magnetic field. Ferric porphyrins have a 3d<sup>5</sup> electron arrangement and a distorted square pyramidal geometry, which results in an  $S = 5/2$  spin system and significant ZFS. The ZFS provides an additional spectroscopic handle since it is sensitive to the coordination environment. The magnetic properties of ferric porphyrins can be described by the following spin Hamiltonian (SH, eq 1)

$$\hat{H} = D \left( \hat{S}_z^2 - \frac{1}{3} \hat{S}^2 \right) + E (\hat{S}_x^2 - \hat{S}_y^2) + \mu_B B_0 \cdot \mathbf{g} \cdot \hat{S} \quad (1)$$

The SH as shown contains two magnetic field-independent terms. The first describes the axial ZFS (as depicted in Scheme 2), which is defined by  $D$ , and splits the 6-fold degenerate  $S = 5/2$  multiplet into three doublets (*viz.*,  $M_S = \pm 1/2, \pm 3/2$ , and  $\pm 5/2$ ). An energy difference of  $2D$  separates the ground state from the first excited doublet ( $\pm 1/2$  to  $\pm 3/2$ ), while  $4D$  separates the second from the third excited doublets ( $\pm 3/2$  to  $\pm 5/2$ ). The second term shown in the SH describes the rhombic ZFS, defined by the parameter,  $E$ , which changes the energies (and wave functions) but does not split the doublets due to Kramer's theorem. By convention, the coordination frame is chosen such that  $|E/D| \leq 1/3$ . The third term describes the Zeeman interaction, *i.e.*, the interaction between spins and the external magnetic field ( $B_0$ ), with  $\mu_B$  being the Bohr magneton. The tensor  $\mathbf{g}$  is approximated as axial in the ZFS frame, *i.e.*,  $\mathbf{g} = \text{diag}(g_{\perp}, g_{\perp}, g_{\parallel})$ , with  $\perp$  and  $\parallel$  referring to the main ZFS axis.

The determination of the axial ZFS parameter,  $D$ , of ferric porphyrins has been the subject of many papers utilizing a variety of techniques, including infrared spectroscopy (IR), Mössbauer spectroscopy, inelastic neutron scattering (INS), and electron paramagnetic resonance (EPR). The rhombic ZFS is typically small/negligible for these complexes, meaning it is often not detected at all,<sup>21–23</sup> leading most studies to focus on the axial ZFS component. Key early work examining ZFS

**Scheme 2.** (A) Spin Energy Diagram of the  $S = 5/2$  Multiplet Absent an External Magnetic Field<sup>a</sup> and (B and C) the Splitting of the Ground State Doublet with an Applied Magnetic Field for  $g_{\perp} = g_{\parallel}$  and  $D > 0$ , in the Low-Field Limit ( $\mu_B B_0 \ll D$ ) and Intermediate Region ( $\mu_B B_0 \lesssim D$ )<sup>b</sup>



<sup>a</sup>The six states are degenerate in the absence of ZFS ( $D$  and  $E = 0$ ). The multiplet is split into three doublets if the ZFS is solely axial ( $D \neq 0$  and  $E = 0$ ) and  $M_S$  is a good quantum number (with  $M_S$  the eigenvalue of the operator  $\hat{S}_z$ ). A positive  $D$  results in a ground state doublet formed by the states with  $M_S = \pm 1/2$ . The  $M_S = \pm 3/2$  doublet is  $2D$  higher in energy, while the  $M_S = \pm 5/2$  doublet is a further  $4D$  higher. EPR transitions are only allowed between states differing in  $M_S$  by 1, with the allowed zero-field transitions denoted as I and II (blue and red arrows, respectively). <sup>b</sup>In both cases, the splitting is different for magnetic fields applied along (solid black line) or perpendicular (dashed red line) to the magnetic  $z$ -axis of the molecule. Allowed EPR transitions,  $III_{\parallel}$  and  $III_{\perp}$ , are shown as green arrows positioned at magnetic fields such that they have an identical transition energy (frequency). The allowed EPR transitions differ in resonance field (despite  $g_{\perp} = g_{\parallel}$  for the  $S = 5/2$  multiplet), due to the presence of  $D$ . In the low-field limit, they are in first order perturbation theory given by  $h\nu_{III_{\perp}} = 3g_{\perp}\mu_B B_0$  and  $h\nu_{III_{\parallel}} = g_{\parallel}\mu_B B_0$ . The former is often referred to as an effective  $g = 6$  signal and characteristic for ferric porphyrins.

for ferric coordination complexes employed IR,<sup>24,25</sup> including a focus on biochemically relevant ferric porphyrins.<sup>26,27</sup> This included studies of met-myoglobin wherein  $D = 9.5(2) \text{ cm}^{-1}$  was found, which decreases to  $D = 5.94(8) \text{ cm}^{-1}$  by exchanging the aquo for a fluoro ligand.<sup>26</sup> The corresponding met-hemoglobin with a  $F^-$  ligand showed  $D = 6.3(1) \text{ cm}^{-1}$ .<sup>26</sup> These values have been more recently confirmed by EPR as  $D = 9.2(4) \text{ cm}^{-1}$  for met-myoglobin, while the fluoro ligand decreases this to  $D = 5.0(1) \text{ cm}^{-1}$ .<sup>17</sup> The corresponding values for met-hemoglobin were  $D = 10.4(2) \text{ cm}^{-1}$  ( $H_2O$ ) and  $D = 5.1(1) \text{ cm}^{-1}$  ( $F^-$ ).<sup>17</sup>

A well-studied example of ZFS determination for ferric porphyrins is ferric tetraphenylporphyrin chloride,  $[Fe(TPP)Cl]$  (Scheme 1), for which Mößbauer spectroscopy indicated  $D = 7(1) \text{ cm}^{-1}$ ,<sup>28</sup> while a more recent determination was made

using INS for  $D = 6.33(8) \text{ cm}^{-1}$ .<sup>29</sup> The groups of Neese and Xue have systematically examined  $D$  for  $[Fe(TPP)X]$ , where  $X$  is  $F^-$ ,  $Cl^-$ ,  $Br^-$ , and  $I^-$  and  $D$  was respectively determined as 4.49(9), 6.33(8), 8.8(2) ( $E = 0.1(2)$ ), and 13.4(6) ( $E = 0.3(2) \text{ cm}^{-1}$ ).<sup>18</sup> For the closely related ferric octaethylporphyrin chloride,  $D = 8(1) \text{ cm}^{-1}$  was found by Mößbauer spectroscopy,<sup>28</sup> while  $D = 7 \text{ cm}^{-1}$  was later concluded by EPR.<sup>30</sup> The group of Franke employed scanning tunnelling microscopy (STM) to determine  $D$  as ca.  $6 \text{ cm}^{-1}$  when the same porphyrin was grafted onto a superconducting Pb surface.<sup>31</sup> Considering other ferric porphyrin chlorides, the group of Ohta has used EPR to determine  $D = 7.2 \text{ cm}^{-1}$  and  $E = 0.0 \text{ cm}^{-1}$  for hemin ( $Fe^{III}$  protoporphyrin IX chloride),<sup>21</sup> which was subsequently refined to  $D = 6.90(1) \text{ cm}^{-1}$  and  $|E| = 0.055(5) \text{ cm}^{-1}$ .<sup>22</sup>

EPR is the ideal method to examine the magnetic properties of transition metal ions,<sup>32,33</sup> and is exceptionally powerful for bioinorganic chemistry.<sup>34–37</sup> This includes work on oxygenated hemoglobin and myoglobin, which allowed the determination of the haem group orientation relative to the protein prior to the availability of suitable diffraction patterns.<sup>38,39</sup> EPR probes unpaired electrons, and in principle the ZFS can be directly measured by EPR. However, conventional EPR is unable to precisely determine a ZFS that is much larger than the incident microwave frequency/energy of the spectrometer. This requirement makes variable frequency EPR and frequency-domain EPR very promising though instrumentally challenging. For a ferric cation with positive  $D$  (and  $E = 0$ ), transitions between the ground state and the first excited doublet (transition I,  $M_S = \pm 1/2$  to  $\pm 3/2$ ) as well as between the first and second excited doublet (transition II,  $M_S = \pm 3/2$  to  $\pm 5/2$ ) can be observed at zero field (Scheme 2A). Measurements at elevated temperatures are necessary to observe the latter transition (II), and the observation of both transitions I and II is required to determine both  $D$  and  $E$  in zero field. A negative  $D$  results in an inversion of the energy levels and consequently to a reversed temperature dependence of transition I and II, i.e., transition II can be observed at lowest temperatures, while elevated temperatures are required to observe transition I. The sign of  $D$  can therefore be clearly determined from the temperature dependence of transitions I and II (Scheme 2A). Ferric porphyrins usually have positive  $D$  values, so subsequent discussion will focus on this scenario. The application of a magnetic field splits the doublets resulting in EPR allowed transitions within the ground state. Depending on the orientation of the molecule (and consequently its magnetic axis), the magnetic field value at which a certain transition energy is reached can differ quite strongly. If the applied field energy is much lower than  $D$  ( $\mu_B B_0 \ll D$ ), then the splitting of the doublet is approximately linear with the magnetic field (Scheme 2B) and similar to an  $S = 1/2$  system, thus allowing effective  $g$  tensors to be introduced.<sup>40</sup> The fingerprint-like signals in X-band EPR spectra of ferric porphyrins at around 115 and 340 mT ( $III_{\perp}$  and  $III_{\parallel}$ ) correspond to effective  $g$  values of around 6 and 2. However, if the energy of the applied field approaches  $D$  ( $\mu_B B_0 \lesssim D$ , e.g., for larger magnetic fields), the splitting deviates from linear field dependency (Scheme 2C),<sup>17,40</sup> which allows the magnitude of  $D$  to be estimated. The presence of a significant rhombic component to the ZFS,  $E$ , induces splitting of transition  $III_{\perp}$ . Hence, the observation of two nearby resonances at low fields allows  $|E/D|$  to be determined.

Ferric porphyrins are examined herein with a combination of EPR approaches to provide a full data set for analysis. For this approach, measurements were undertaken at X-band (*ca* 9.5 GHz), J-band (263 GHz), multi-high-frequency EPR (MHF-EPR) and with frequency-domain Fourier-transform THz-EPR (FD-FT THz-EPR). MHF-EPR in transmission mode with frequency multipliers allows for a series of measurements at high frequencies (79–629 GHz used herein). FD-FT THz-EPR allows EPR analysis in the frequency domain under a varied magnetic field, with frequencies from 150 GHz to 1.2 THz (5 to 40  $\text{cm}^{-1}$ ).<sup>17,33,41,42</sup> An excitation energy range from the microwave through to far-infrared means both spin transitions and soft vibrational modes may be excited, though these absorptions are separated by measuring their magnetic field dependence.<sup>33</sup> Thus, the frequency dependent absorption is first measured absent an external magnetic field and then repeated at applied fields, confirming the magnetic transitions. Comparing experimental and simulated spectra across multiple frequencies and fields allows the accuracy of the simulation parameters to be thoroughly scrutinized.

The analysis is focused on ferric hemo porphyrins, along with complementary planar porphyrins, to examine fine-tuning of the porphyrin electronics and effects of the hanging group. This is key to establishing if improved catalytic activity observed by hemo porphyrins is due to the Brønsted acid/base group, or if changes in porphyrin electronic structure also contribute. The studied ferric hemo porphyrins have architectures based on tetramesitylporphyrin with a xanthene pillar functionalized with either a carboxylic acid or a methyl carboxylate ([Fe(HPX-COOH)Cl] and [Fe(HPX-COOMe)-Cl] respectively, where HPX is hemo porphyrin xanthene and Me = methyl; Scheme 1). Changes to the porphyrin substituents in either the meso- or  $\beta$ -position alter the electronics, so for comparison and completeness, *D* was also determined for a systematic series of ferric porphyrins with axial chlorides (Scheme 1), where the porphyrin is tetraphenylporphyrin (TPP), octaethylporphyrin (OEP), tetramesitylporphyrin (TMP), or tetra(pentafluorophenyl)porphyrin (TPFPP).

## RESULTS

Focusing initially on the [Fe(OEP)Cl] FD-FT THz-EPR spectra, the magnetic field dependence of signals was examined from 0 to 7 T at a temperature of 2.5 K, along with the temperature dependence at four cryogenic temperatures with applied fields of 0 and 7 T. The absorbance spectra at zero-field are obtained by dividing a reference measurement at a higher temperature (30 K) by the measurement at the temperature of interest. The different spin populations of energy levels at the two temperatures lead to the observation of absorbance (as discussed in a recent review<sup>41</sup> and described briefly in the Experimental Section herein). The 7.5–35  $\text{cm}^{-1}$  energy range was chosen due to the vanishing intensity of the raw spectra at lower energies (see Figure S1). The absorbance spectra at zero-field display a maximum at 14.1  $\text{cm}^{-1}$  that decreases with temperature, as well as a minimum at 27.3  $\text{cm}^{-1}$  that increases with temperature (Figure 1, lower). These can be directly identified as transitions I and II, respectively (Scheme 2A), from which *D* and *E* may be determined. However, this is inaccurate as the line shape of I is distorted, probably due to overlap with a nonmagnetic absorption that is partially resolved at 16 K. I is observed as a maximum that exhibits decreasing absorbance with increasing temperature, as

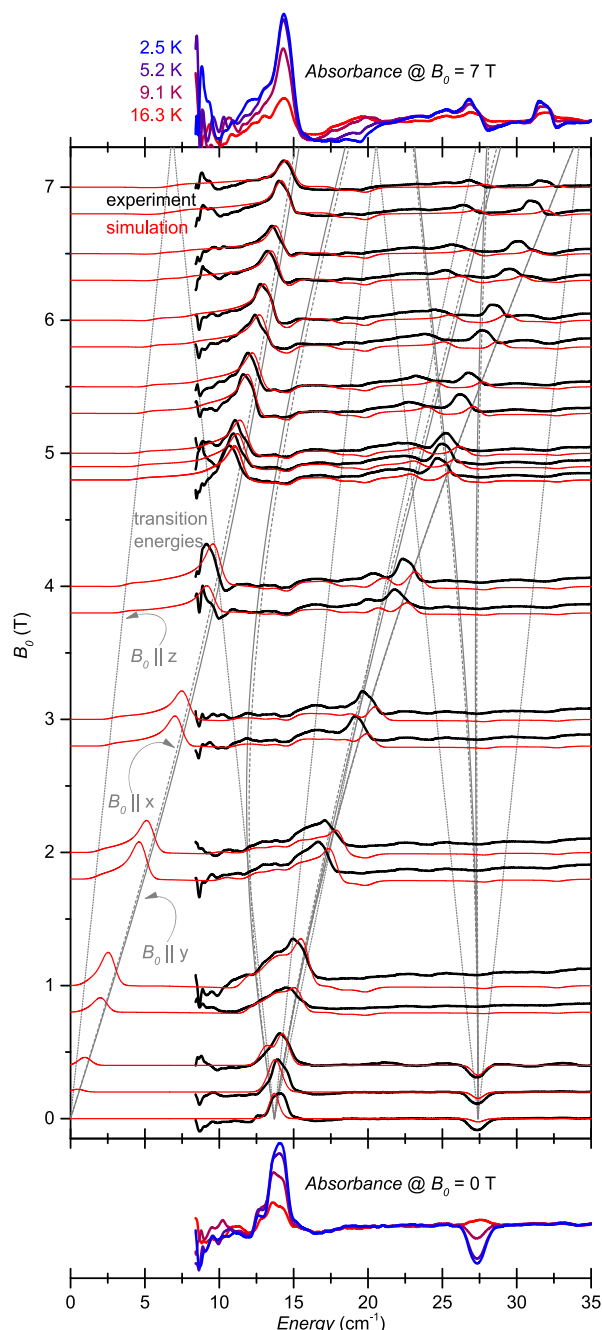


**Figure 1.** FD-FT THz-EPR absorbance spectra of [Fe(OEP)Cl] at magnetic fields of 7 T (top) and 0 T (bottom) with the indicated temperatures. The main panel shows spectra offset to the corresponding magnetic field and measured at a temperature of 2.5 K. These spectra were divided by a reference spectrum measured at 0 T and 30 K (fields below 0.5 T) or 7 T and 30 K (spectra measured at >0.5 T), as specified in Table S1. Experimental spectra (black) are overlaid on simulations (red; simulation parameters specified in Table 1). Simulated transition energies for magnetic fields parallel to the *x* (dashed), *y* (solid), and *z* (dotted) axes are shown as gray background lines for transitions that contribute significantly to the simulated spectra.

the absorption is highest at low temperatures. This is the opposite of II, which displays the highest absorption at elevated temperatures. At low temperatures, although there is minor absorption, this is observed as minimum in the absorbance spectrum, due to the much stronger absorption

in the reference spectrum (30 K). This temperature dependence of I and II is synonymous with a positive  $D$  value.

Under application of a magnetic field, the line arising from transition I broadens in an unsymmetrical manner (main panel of Figure 1). The influence of the applied field upon the line shape clearly distinguishes it from a nonmagnetic absorption (like vibrations or phonons).

The line arising from transition II is seemingly unaffected by magnetic fields less than 0.5 T and absent from spectra measured with higher fields. This is because spectra measured with magnetic fields less than 0.5 T use the zero-field 30 K reference spectrum, while the measurements at 0.5–7.0 T use a reference measured at 7 T and 30 K. Because the minimum assigned to II is visible due to the reference spectrum (0 T, 30 K), it is seemingly unaffected by the applied field. The signal is identified as an EPR transition by comparison with the high-field reference (7 T, 30 K), in which the signal is shifted to an energy exceeding the analysis range. Furthermore, an additional EPR line is observable at the low end of the energy range when the field is 4–7 T. This signal can be directly assigned to transition III<sub>L</sub>, concordant with simulations, and its nonlinear field dependence indicates  $\mu_B B_0 \lesssim D$  within the measured field range (see Scheme 2C).

MHF-EPR spectra of [Fe(OEP)Cl] all show a strong, slightly split line that displays an increasing resonance field consistent with the increasing frequency (Figures 2 and S2–S4). Its resonance field shifts from 1.0 T at 79 GHz to 11.8 T at 629 GHz concordant with simulations, and it is consequently assigned to transition III<sub>L</sub>. Its nonlinear field dependence indicates  $\mu_B B_0 \lesssim D$  (see Scheme 2C). An additional set of lines is observed at low fields for frequencies around 420 GHz (14 cm<sup>-1</sup>), which can be assigned to transition I. These results are coherent with those from FD-FT THz-EPR with the same simulation parameters used for modeling.

Magnetic parameters were obtained by systematically optimizing simulations in both frequency and field domains against the experimental spectra (Table 1), yielding values of  $g_{\perp}$  and  $g_{\parallel}$  = 1.99(3) and  $D$  = 6.85(5) cm<sup>-1</sup> for [Fe(OEP)Cl]. The uncertainties were also estimated heuristically by individually varying each parameter in simulations and comparing the agreement with experimental spectra. Simulations of FD-FT THz-EPR absorbance visually disagree in the position of the zero-field maximum, which is likely due to the aforementioned overlap with a nonmagnetic resonance. The final simulation parameters result in overall excellent agreement with the experimental MHF-EPR spectra (Figure 2), and the mismatch for a few relative intensities is probably due to the presence of microcrystallites in the sample (vs a perfect powder).

The FD-FT THz-EPR spectra of [Fe(TMP)Cl] resemble those of [Fe(OEP)Cl] with slight shifts of the peak energies (cf. Figure 3 and Figure 1; note that, due to technical reasons, the spectra are shown as magnetic division spectra (MDS) and absorbance, respectively; raw spectra are shown in Figure S5).

[Fe(TMP)Cl] was investigated with field-domain EPR at frequencies in X- and J-bands. The X-band EPR spectrum was observed as typical for an  $S = 5/2$  system with large axial ZFS (Figure 4). A strong EPR line at 115 mT dominates the spectrum, while a weaker line is observed at 340 mT (the additional signal at 160 mT was assigned to an impurity). Simulations indicate these two lines are due to transitions III<sub>L</sub> and III<sub>H</sub>, respectively (Scheme 2C). A line at 3.6 T was

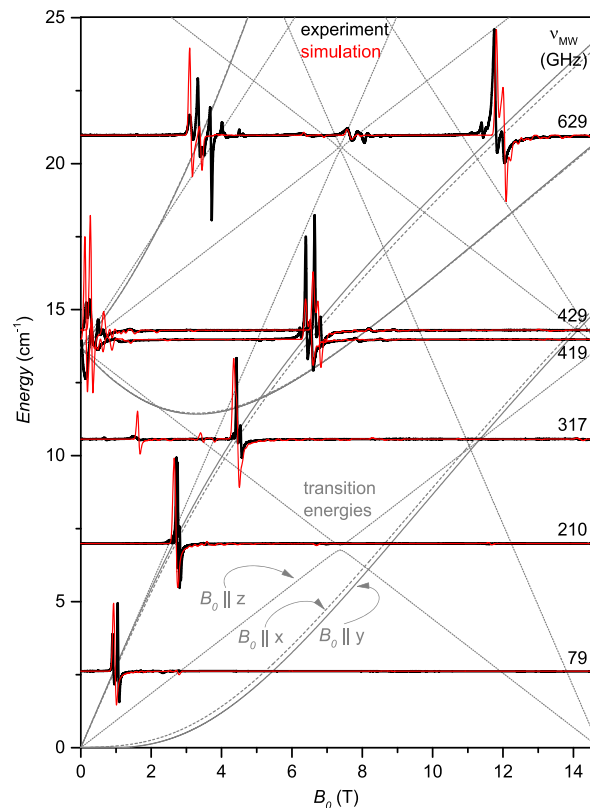


**Figure 2.** MHF-EPR spectra of [Fe(OEP)Cl]. Spectra are rescaled for visibility and offset according to the MW energy at which they were measured with the frequency indicated. Experimental spectra (black) are overlaid on simulations (red; simulation parameters specified in Table 1). Simulated transition energies for magnetic fields parallel to the  $x$  (dashed),  $y$  (solid), and  $z$  (dotted) axes are shown as gray background lines for transitions that contribute significantly to the simulated spectra. All spectra were measured at 5 K.

**Table 1. Magnetic Parameters Determined Herein Using eq 1**

ferric porphyrin <sup>a</sup>	$D/\text{cm}^{-1}$	$ E/D $	$g_{\perp}$	$g_{\parallel}$
[Fe(TPP)Cl] <sup>b</sup>	6.465(3)	0.003(2)	2.00(5)	1.95(5)
[Fe(OEP)Cl]	6.85(5)	0.003(1)	1.99(3)	
[Fe(TMP)Cl]	6.30(4)	0.000(5)	1.992(5)	1.984(5)
[Fe(TPFPP)Cl]	6.24(8)	0.00(2)		1.98(5)
[Fe(HPX-COOH)Cl]	6.6(2)	0.00(2)	2.019(5)	2.005(5)
[Fe(HPX-COOMe)Cl]	6.55(3)	0.00(1)	2.024(5)	2.005(5)

<sup>a</sup>Chemical structures of each complex depicted in Scheme 1. <sup>b</sup>Values from a previous study using the same techniques.<sup>23</sup>

observed in the J-band spectrum and assigned to III<sub>L</sub>, while the line corresponding to III<sub>H</sub> is expected to be much weaker than the III<sub>L</sub> line (based on the X-band EPR spectrum) and was not observed. Neither at X- nor J-band was a splitting of III<sub>L</sub> observed, which provides an upper limit for the  $|E/D|$  ratio of 0.005. For an axial  $S = 5/2$  system where  $D \gg 0.33 \text{ cm}^{-1}$  (10 GHz),  $g_{\perp}$  and  $g_{\parallel}$  can be directly obtained from the X-band spectrum and are assigned as 1.992(5) and 1.984(5), respectively (Table 1). The  $D$  value can be read off the FD-FT THz-EPR absorbance spectrum at zero field as 6.30(4) cm<sup>-1</sup>. Simulations with these parameters accurately reproduce

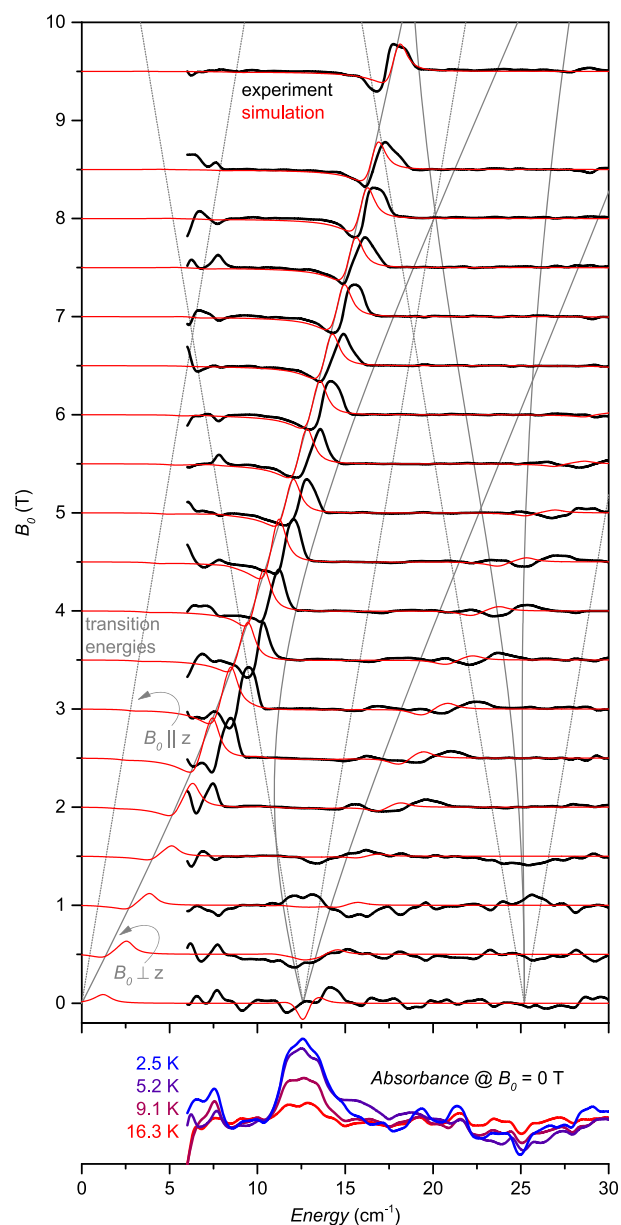


**Figure 3.** Main panel: FD-FT THz-EPR magnetic division spectra of [Fe(TMP)Cl]. Spectra are offset to the corresponding magnetic field and measured at a temperature of 2 K. Experimental spectra (black) are overlaid on simulations (red; simulation parameters specified in Table 1). Simulated transition energies for magnetic fields parallel (dotted) and perpendicular (solid) to the  $z$  axis are shown as gray background lines for transitions that contribute significantly to the simulated spectra. The absorbance at the indicated temperatures absent an applied magnetic field is shown in the bottom panel.

the field-domain EPR spectra (Figure 4), though it is not understood why they diverge from the FD-FT THz-EPR MDS spectra (Figure 3). [In the simulation of the X-band EPR spectrum, a 4.9(5)% impurity was included with  $S = 3/2$ , large  $D$  ( $6.3\text{--}10\text{ cm}^{-1}$ ),  $g_{\perp} = 2.16(1)$ , and  $g_{\parallel} = 2.01(1)$ .]

[Fe(TPFPP)Cl] was probed with FD-FT THz-EPR and exhibited spectral features comparable to those of [Fe(OEP)Cl] and [Fe(TMP)Cl] (see SI, Figures S6 and S7). Simulations of the FD-FT THz-EPR spectra allowed the spectra to be well reproduced using  $g_{\perp}$  and  $g_{\parallel}$  equal to 1.98(5) and a  $D$  of  $6.24(8)\text{ cm}^{-1}$  (Table 1).

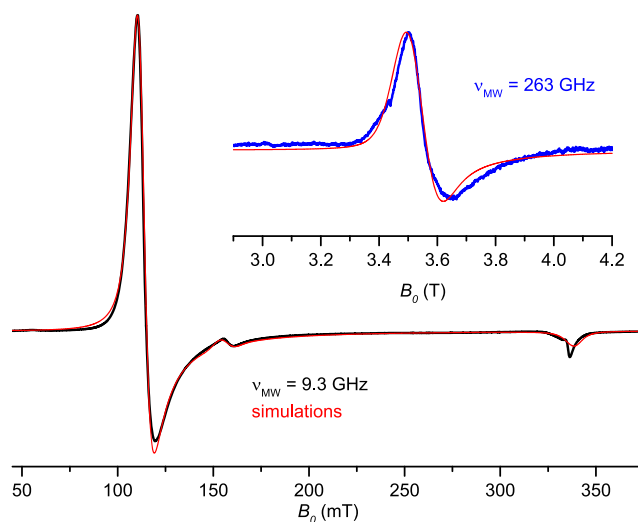


**Figure 4.** Field-domain EPR spectra of [Fe(TMP)Cl]. The X-band EPR spectrum (black line) and the relevant region of the J-band EPR spectrum (blue line on inset axis) are shown overlaid upon simulations (red lines).  $T = 5\text{ K}$  for both experiments.

The hangman porphyrin [Fe(HPX-COOMe)Cl] shows comparable spectral features to the aforementioned [Fe(TMP)Cl], though the resonance positions are slightly shifted in the FD-FT THz-EPR and X-band spectra (Figures 5, S8, and S9, respectively). The obtained magnetic parameters are of course also similar (Table 1), with simulations using  $D = 6.55(3)\text{ cm}^{-1}$  and  $g_{\perp}$  and  $g_{\parallel}$  as 2.024(5) and 2.005(5), yielding spectra concordant with the experimental results. The second hangman porphyrin, [Fe(HPX-COOH)Cl], revealed rather weak EPR lines by FD-FT THz-EPR and at X-band (Figures S10, S11, and S12). The resonance positions very closely resemble those observed for [Fe(HPX-COOMe)Cl], and consequently the magnetic parameters show only small differences (Table 1).

## DISCUSSION

Ferric porphyrin chlorides typically exhibit positive axial ZFS parameters of  $D = 6\text{--}7\text{ cm}^{-1}$ , with a rhombic ZFS component of  $E < 1\text{ cm}^{-1}$ .<sup>17,18,21–23,28,29</sup> All the complexes analyzed herein fall into this expected range, including the hangman structures (see Table 1). The subtle differences in ZFS due to changes in the porphyrin substituents were able to be determined due to the sensitivity of the employed approach. These types of structural modifications have been described as providing the ability to fine-tune the catalytic activity of metalloporphyrins, while the presence of a hangman group has a more significant influence on catalytic activity.

[Fe(OEP)Cl] was herein determined to have a  $D$  value of  $6.85(5)\text{ cm}^{-1}$ , which is comparable to the literature value for hemin (Fe<sup>III</sup> protoporphyrin IX chloride) of  $6.90(1)\text{ cm}^{-1}$ .<sup>22</sup> These values are significantly higher than  $D$  for [Fe(TPP)Cl], which has been examined in great detail using complementary techniques (*vide supra*), with  $6.465(3)\text{ cm}^{-1}$  having been determined by FD-FT THz-EPR.<sup>23</sup> These values are also consistent with previous findings that the ZFS was higher for [Fe(OEP)Cl] than [Fe(TPP)Cl].<sup>28</sup>

Exchanging the phenyl substituents of [Fe(TPP)Cl] for mesityl substituents gives the structurally similar but sterically more congested [Fe(TMP)Cl], for which  $D = 6.30(4)\text{ cm}^{-1}$

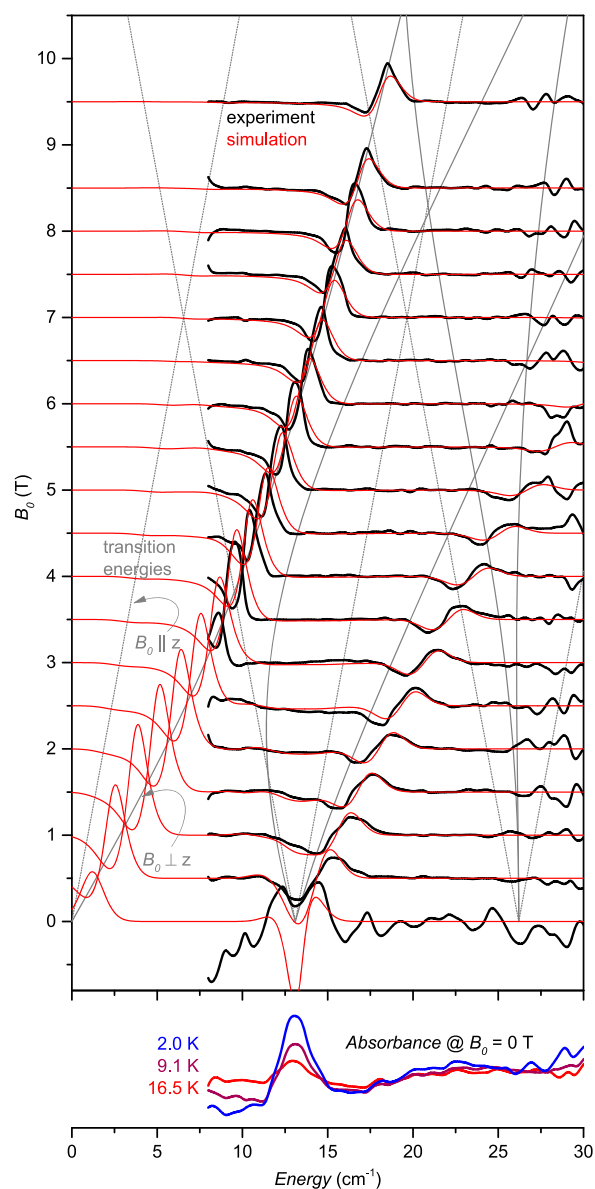


**Figure 5.** Main panel: FD-FT THz-EPR magnetic division spectra of [Fe(HPX-COOMe)Cl]. Spectra are offset corresponding magnetic field and measured at a temperature of 2 K. Experimental spectra (black) are overlaid on simulations (red; simulation parameters specified in Table 1). Simulated transition energies for magnetic fields parallel (dotted) and perpendicular (solid) to the  $z$  axis are shown as gray background lines for transitions that contribute significantly to the simulated spectra. The absorbance at the indicated temperatures absent an applied magnetic field is shown in the bottom panel.

was determined herein. To systematically probe the effect of a stronger electron withdrawing substituent on the porphyrin electronics, the phenyl moiety was also exchanged for the penta-fluorinated variant to yield [Fe(TPFPP)Cl]. This had the effect of lowering the measured  $D$  value to  $6.24(8) \text{ cm}^{-1}$ . These three values do not indicate a correlation of  $D$  with the electron donating/withdrawing character in the porphyrin substituents (TMP, TPP, TPFPP). This is probably because the steric bulk of the aromatic substituents ensures they are near perpendicular to the porphyrin plane (crystal structures exist for the latter two),<sup>43–45</sup> thus hindering their conjugation with the  $\pi$  orbitals of the porphyrin. The more subtle electronegativity effect through the  $\sigma$  bonds likely explains

the similarity of  $D$  and gives an indication of the magnitude of catalytic fine-tuning.

The aforementioned study of [Fe(TPP)X] by Neese and colleagues showed that larger halogens ( $X = \text{F}^-$ ,  $\text{Cl}^-$ ,  $\text{Br}^-$ ,  $\text{I}^-$ ) and consequently softer ligands systematically increase the axial ZFS ( $D = 4.49(9)$ ,  $6.33(8)$ ,  $8.8(2)$ ,  $13.4(6) \text{ cm}^{-1}$ , respectively).<sup>18</sup> It is elegantly described therein that  $D$  is correlated with the increasingly covalent nature of the Fe–X bond, and with larger spin orbit coupling. Indeed, the length of the Fe–X bond increases along the series from  $1.79$ ,<sup>46</sup> to  $2.21$ ,<sup>43</sup> to  $2.35$ ,<sup>47</sup> to  $2.55 \text{ \AA}$ ,<sup>48</sup> while the Fe displacement from the  $N_4$  plane is essentially unchanged at  $0.48 \pm 0.02 \text{ \AA}$  (Table 2).<sup>43,46–48</sup> Work by Franke and colleagues on [Fe(OEP)Cl] using an STM tip to attract the chloride also indicated that increasing the Fe–X bond length led to an increase in  $D$ .<sup>31,49</sup>

**Table 2.** Selected Crystal Structure Parameters for Ferric Porphyrins Taken from the Literature

ferric porphyrin	Fe–halide bond distance/ $\text{\AA}$	Fe displacement from plane/ $\text{\AA}$
[Fe(TPP)F] <sup>46</sup>	1.79	0.47
[Fe(TPFPP)Cl] <sup>44,45</sup>	2.19	0.45
[Fe(TPP)Cl] <sup>43</sup>	2.21	0.49
[Fe(PPIX)Cl] <sup>450</sup>	2.22	0.48
[Fe(OEP)Cl] <sup>51,52</sup>	2.23	0.49
[Fe(TPP)Br] <sup>47</sup>	2.35	0.49
[Fe(TPP)I] <sup>48</sup>	2.55	0.46

<sup>a</sup>PPIX = protoporphyrin IX.

Correlations between bond lengths and  $D$  values were also explored herein and extrapolated to include porphyrin structures where crystal structures are hitherto not available. [Fe(OEP)Cl] crystallizes with a  $2.23 \text{ \AA}$  Fe–Cl bond,<sup>51,52</sup> while for hemin the length is  $2.22 \text{ \AA}$ .<sup>50</sup> Both have  $D$  values that are relatively high for ferric porphyrin chlorides, and slightly longer axial bonds than [Fe(TPP)Cl]. The Fe–Cl bond length in [Fe(TPFPP)Cl] is  $2.19 \text{ \AA}$ ,<sup>44</sup> with the lower  $D$  value accompanying a shorter bond length. Regrettably, a crystal structure could not be found for [Fe(TMP)Cl], though the  $D$  value supports a logical and intuitive Fe–Cl distance between those of [Fe(TPFPP)Cl] and [Fe(TPP)Cl] (i.e.,  $2.20 \text{ \AA}$ ).

The carboxylic acid and methyl carboxylate functionalized hangman porphyrins examined herein were determined to have respective  $D$  values of  $6.6(2)$  and  $6.55(3) \text{ cm}^{-1}$  ([Fe(HPX-COOH)Cl] and [Fe(HPX-COOMe)Cl] in Table 1). The hangman porphyrins are structurally equivalent to the planar [Fe(TMP)Cl], aside from the replacement of a mesityl substituent with the hangman pillar (Scheme 1). Consequently, as for the planar porphyrins, strong electron donation or withdrawal via the aromatic  $\pi$  orbital system is prohibited by the sterically enforced angle of the bulky porphyrin substituents. However,  $D$  is significantly higher for the hangman functionalized porphyrins than [Fe(TMP)Cl] ( $6.6$  vs  $6.3 \text{ cm}^{-1}$ ), indicating they have Fe–Cl bond lengths between those of [Fe(TMP)Cl] and [Fe(OEP)Cl] (i.e.,  $2.20$ – $2.23 \text{ \AA}$ ).

Unfortunately, no crystal structures are available for ferric hangman porphyrins with chloride axial ligands, though one exists for the equivalent structure with an axial hydroxyl ligand.<sup>11</sup> Therein, the hangman group and axial ligand are located on the same porphyrin plane, with water present between the hangman group and axial ligand. A similar

hydrogen bonding arrangement could be considered here, whereby hydrogen bonding withdraws electron density to make  $\text{Cl}^-$  a softer ligand and thus increases  $D$ . Hydrogen bonding has been shown to increase Fe–Cl bond lengths from 2.23 to 2.36 Å (comparable to an Fe–Br bond) in octaethyltetraarylporphyrin.<sup>53</sup> However, an Fe–Cl bond length outside the typical ferric porphyrin chloride range is incoherent with the  $D$  values measured herein, thus implying that any hydrogen bonding effects are weaker in the hangman porphyrins than in the aforementioned study. It may also be expected that the strength of such an interaction would vary between the carboxylic acid and methyl carboxylate moieties, though it is interesting that no significant difference in  $D$  was detected.

It is also possible that the changes in  $D$  are due to the different electronics of the xantheno pillar compared to the mesityl group, in the same manner that changing the phenyl substituents to mesityl or pentafluorophenyl groups induced a change in  $D$  of the same order (*vide supra*). In this scenario,  $D$  would be largely insensitive to changing the hangman moiety from a carboxylic acid to a methyl carboxylate, which is consistent with the determined values.

## CONCLUSION

A series of ferric porphyrin chlorides was studied with FD-FT THz-EPR and field domain EPR at frequencies between 9.3 and 629 GHz. This allowed subtle differences in the magnetic properties to be distinguished and values determined with high accuracy. The experimentally obtained  $D$  values span a range from 6.24 to 6.85  $\text{cm}^{-1}$ , with vanishing rhombicity (maximum  $|E/D| = 0.003$ ). Changes to the porphyrin substituents, including the presence of a hangman motif, did not shift the ZFS parameters beyond this range. The accuracy of the employed techniques in determining  $D$  values allowed correlations with Fe–halide bond lengths to be examined for different porphyrin chlorides rather than different halides. This correlation prompted estimates of the Fe–Cl bond length based on the  $D$  values of the hangman porphyrins for which no crystal structures are known. The high precision of the combination of FD-FT THz-EPR and field domain EPR over a wide range of frequencies has thus been exemplified for ferric porphyrins in particular.

## EXPERIMENTAL SECTION

**FD-FT THz-EPR.** Frequency domain Fourier transform EPR (FD-FT THz-EPR) spectroscopy experiments were conducted on the THz beamline of the BESSY II storage ring, at the dedicated end station that has been described elsewhere in detail,<sup>33,42</sup> and recently reviewed.<sup>41</sup> Briefly, radiation is passed through an FT-IR spectrometer (Bruker IFS 125), to be then transmitted through the sample placed in the variable-temperature insert inside an optical magnet (Oxford Optistat) and finally detected by a Si bolometer (Infrared Laboratories, Far-Infrared bolometer) cooled down to 1.3 K. Radiation used was either from a Hg-arc lamp ( $[\text{Fe}(\text{OEP})\text{Cl}]$ ) or coherent synchrotron radiation extracted from BESSY II operated in low- $\alpha$  storage-ring mode (all other porphyrins). The FT-IR spectrometer was operated with resolution of 0.5  $\text{cm}^{-1}$  and Mylar beam splitter of 50 ( $[\text{Fe}(\text{OEP})\text{Cl}]$ ,  $[\text{Fe}(\text{TPFPP})\text{Cl}]$ ) or 23  $\mu\text{m}$  ( $[\text{Fe}(\text{TMP})\text{Cl}]$ ,  $[\text{Fe}(\text{HPX-COOMe})\text{Cl}]$ ,  $[\text{Fe}(\text{HPX-COOH})\text{Cl}]$ ) thickness. The detected signal is the power of the transmitted radiation as a function of frequency. To account for varying spectral density etc., a reference is required. In traditional FT-IR spectroscopy, often a blank spectrum is used. The strong nonmagnetic absorption forbids this for FD-FT THz-EPR. Therefore, spectra of the sample under varied experimental conditions are used. Here, we used absorbance ( $A = \log_{10}(I_{\text{ref}}/I_0)$ ), with  $I_0$  the spectrum of interest and  $I_{\text{ref}}$

the reference spectrum) and magnetic field division spectra (MDS,  $M = [I(B_0)]/[I(B_0 + 0.5T)]$ , with  $I(x)$  the spectrum measured at the magnetic field  $x$  and both spectra measured at the same temperature). The expected shapes of such obtained spectra are described in ref 41.  $I_{\text{ref}}$  for absorbance spectra was measured at a temperature of 30 K and in the absence of a magnetic field, except for absorbance spectra of  $[\text{Fe}(\text{OEP})\text{Cl}]$  with magnetic fields of more than 0.5 T. For those,  $I_{\text{ref}}$  was measured at 30 K and 7 T.

**MHF-EPR.** Multi-high-frequency EPR (MHF-EPR) was measured at the EMR facility of the National High Magnetic Field Laboratory, Tallahassee, FL. A transmission type spectrometer with a phase-locked Virginia Diodes source combined with a series of frequency multipliers, covering the range from 50 to 635 GHz, was used.<sup>54</sup> The sample is placed inside a 17 T superconducting magnet (Oxford) equipped with a continuous-flow cryostat. The signal was field-modulated at 50 kHz and 10 G amplitude. For detection, an InSb electron bolometer (QMC) was used.

**J-band EPR** was performed on a Bruker Elexsys E780 EPR spectrometer using a nonresonant sample insert and a continuous-flow cryostat. Experiments were performed at a temperature of 5 K. MW frequency was 262.354 GHz, and the nominal output power was 15 mW. Field modulation at 100 kHz with 40 G amplitude was used.

**X-band EPR** was performed on a Bruker ESP300, equipped with a continuous flow cryostat and a  $\text{TE}_{011}$  super high Q resonator. Spectra were measured at a temperature of 5 K and with field modulation at 100 kHz with 10 G amplitude. MW frequencies and powers were 9.393, 9.392, and 9.392 GHz and 0.8, 0.8, and 0.2 mW for  $[\text{Fe}(\text{TMP})\text{Cl}]$ ,  $[\text{Fe}(\text{HPX-COOMe})\text{Cl}]$ , and  $[\text{Fe}(\text{HPX-COOH})\text{Cl}]$ , respectively.

**EPR spectra simulations** employed the Matlab toolbox, *EasySpin*,<sup>55</sup> with FD-FT THz-EPR utilizing a recently developed frequency-domain extension included therein.<sup>23,56</sup>

**Preparation of Samples for Analysis.** FD-FT THz-EPR experiments were performed using pellets of 10 mm diameter.  $[\text{Fe}(\text{OEP})\text{Cl}]$  was mixed with polyethylene (PE), ground, and pressed into a pellet. The other porphyrins were dissolved in acetone; PE was added to the solution and the solution dried out and pressed into a pellet. For MHF-EPR, ground powder of  $[\text{Fe}(\text{OEP})\text{Cl}]$  was filled into a plastic holder, closed with a Teflon cap. For J-band EPR experiments,  $[\text{Fe}(\text{TMP})\text{Cl}]$  in acetone solution was filled in the Teflon sample holder. After the acetone was dried off, the lid was closed. X-band EPR experiments were performed on acetone solutions filled in X-band quartz tubes.

**Samples.**  $[\text{Fe}(\text{TPP})\text{Cl}]$  was previously measured by Nehrkorn et al.,<sup>23</sup> using the same instrumentation and approach. The sample, chloro(5,10,15,20-tetraphenylporphyrin)iron(III), was purchased from a commercial supplier (Sigma-Aldrich) and used as received (CAS 16456-81-8).  $[\text{Fe}(\text{OEP})\text{Cl}]$ , 2,3,7,8,12,13,17,18-octaethyl-21H,23H-porphine iron(III) chloride, was purchased from a commercial supplier (Sigma-Aldrich) and used as received (CAS 28755-93-3).

**Synthetic Procedure.** The other ferric porphyrins were synthesized according to published procedures that will only be briefly outlined herein. For the hangman porphyrins, the free base porphyrins HPX-COOH and HPX-COOMe were synthesized according to a previously defined microwave synthesis protocol.<sup>57</sup> Subsequent reaction with iron(II) chloride in dimethylformamide and aerobic acid workup yields the corresponding chloroiron(III) porphyrin complexes.<sup>12</sup>  $[\text{Fe}(\text{TMP})\text{Cl}]$  and  $[\text{Fe}(\text{TPFPP})\text{Cl}]$  were synthesized following the same metalation procedure from the known ligands, TMP and TPFPP.<sup>58</sup>

## ASSOCIATED CONTENT

### Supporting Information

The Supporting Information is available free of charge on the ACS Publications website at DOI: 10.1021/acs.inorgchem.9b02348.

Additional spectra for  $[\text{Fe}(\text{OEP})\text{Cl}]$ ,  $[\text{Fe}(\text{TMP})\text{Cl}]$ , and  $[\text{Fe}(\text{HPX-COOMe})\text{Cl}]$ , spectra for  $[\text{Fe}(\text{TPFPP})\text{Cl}]$

and [Fe(HPX-COOH)Cl] as Figures S1–S12 and Table S1 (PDF)

## AUTHOR INFORMATION

### Corresponding Authors

\*E-mail: [Joscha.Nehrkorn@cec.mpg.de](mailto:Joscha.Nehrkorn@cec.mpg.de).

\*E-mail: [Shannon.Bonke@cec.mpg.de](mailto:Shannon.Bonke@cec.mpg.de).

### ORCID

Joscha Nehrkorn: 0000-0003-1156-5675

Shannon A. Bonke: 0000-0002-3285-4356

Matthias Schwalbe: 0000-0003-4209-1601

### Notes

The authors declare no competing financial interest.

## ACKNOWLEDGMENTS

The authors are grateful to Dr. Samuel M. Greer (National High Magnetic Field Laboratory, FL, USA), Dr. Karsten Hollmack for experimental assistance, Dr. Steffen Meyer for productive discussions on iron chemistry (the latter are affiliated with Helmholtz-Zentrum Berlin, Germany), and Prof. Dr. Katharina J. Franke (Freie Universität Berlin, Germany) for inspiring the work on [Fe(OEP)Cl]. J.N. thanks Prof. Dr. Carmen Herrmann (Universität Hamburg, Germany) for support and discussions. The National High Magnetic Field Laboratory is supported by the National Science Foundation through NSF/DMR-1157490 and the State of Florida. Funding from the Deutsche Forschungsgemeinschaft through SPP 1601 and a research fellowship to J.N. (grant no. NE 2064/1-1) is gratefully acknowledged. S.A.B. gratefully acknowledges a fellowship from the Alexander von Humboldt Foundation.

## REFERENCES

- Rosenthal, J.; Nocera, D. G. Role of Proton-Coupled Electron Transfer in O–O Bond Activation. *Acc. Chem. Res.* **2007**, *40* (7), 543–553.
- Rao, H.; Schmidt, L. C.; Bonin, J.; Robert, M. Visible-light-driven methane formation from CO<sub>2</sub> with a molecular iron catalyst. *Nature* **2017**, *548*, 74–77.
- Collman, J. P.; Fu, L.; Herrmann, P. C.; Zhang, X. A Functional Model Related to Cytochrome c Oxidase and Its Electrocatalytic Four-Electron Reduction of O<sub>2</sub>. *Science* **1997**, *275* (5302), 949.
- Collman, J. P.; Devaraj, N. K.; Decréau, R. A.; Yang, Y.; Yan, Y.-L.; Ebina, W.; Eberspacher, T. A.; Chidsey, C. E. D. A Cytochrome c Oxidase Model Catalyzes Oxygen to Water Reduction Under Rate-Limiting Electron Flux. *Science* **2007**, *315* (5818), 1565.
- Collman, J. P.; Wagenknecht, P. S.; Hutchison, J. E. Molecular Catalysts for Multielectron Redox Reactions of Small Molecules: The “Cofacial Metalloporphyrin” Approach. *Angew. Chem., Int. Ed. Engl.* **1994**, *33* (15–16), 1537–1554.
- Lang, P.; Schwalbe, M. Pacman Compounds: From Energy Transfer to Cooperative Catalysis. *Chem. - Eur. J.* **2017**, *23* (69), 17398–17412.
- Chang, C. J.; Deng, Y.; Heyduk, A. F.; Chang, C. K.; Nocera, D. G. Xanthene-Bridged Cofacial Bisporphyrins. *Inorg. Chem.* **2000**, *39* (5), 959–966.
- Deng, Y.; Chang, C. J.; Nocera, D. G. Direct Observation of the “Pac-Man” Effect from Dibenzofuran-Bridged Cofacial Bisporphyrins. *J. Am. Chem. Soc.* **2000**, *122* (2), 410–411.
- Chang, C. J.; Baker, E. A.; Pistorio, B. J.; Deng, Y.; Loh, Z.-H.; Miller, S. E.; Carpenter, S. D.; Nocera, D. G. Structural, Spectroscopic, and Reactivity Comparison of Xanthene- and Dibenzofuran-Bridged Cofacial Bisporphyrins. *Inorg. Chem.* **2002**, *41* (12), 3102–3109.
- Pistorio, B. J.; Chang, C. J.; Nocera, D. G. A Phototriggered Molecular Spring for Aerobic Catalytic Oxidation Reactions. *J. Am. Chem. Soc.* **2002**, *124* (27), 7884–7885.
- Yeh, C.-Y.; Chang, C. J.; Nocera, D. G. “Hangman” Porphyrins for the Assembly of a Model Heme Water Channel. *J. Am. Chem. Soc.* **2001**, *123* (7), 1513–1514.
- Chang, C. J.; Chng, L. L.; Nocera, D. G. Proton-Coupled O–O Activation on a Redox Platform Bearing a Hydrogen-Bonding Scaffold. *J. Am. Chem. Soc.* **2003**, *125* (7), 1866–1876.
- Chng, L. L.; Chang, C. J.; Nocera, D. G. Catalytic O–O Activation Chemistry Mediated by Iron Hangman Porphyrins with a Wide Range of Proton-Donating Abilities. *Org. Lett.* **2003**, *5* (14), 2421–2424.
- Rosenthal, J.; Chng, L. L.; Fried, S. D.; Nocera, D. G. Stereochemical control of H<sub>2</sub>O<sub>2</sub> dismutation by Hangman porphyrins. *Chem. Commun.* **2007**, *0* (25), 2642–2644.
- McGuire, R., Jr.; Dogutan, D. K.; Teets, T. S.; Suntivich, J.; Shao-Horn, Y.; Nocera, D. G. Oxygen reduction reactivity of cobalt(ii) hangman porphyrins. *Chem. Sci.* **2010**, *1* (3), 411–414.
- Zyska, B.; Schwalbe, M. Synthesis of sterically hindered xanthene-modified iron corroles with catalase-like activity. *Chem. Commun.* **2013**, *49* (36), 3799–3801.
- Nehrkorn, J.; Martins, B. M.; Hollmack, K.; Stoll, S.; Dobbek, H.; Bittl, R.; Schnegg, A. Zero-field splittings in metHb and metMb with aquo and fluoro ligands: a FD-FT THz-EPR study. *Mol. Phys.* **2013**, *111* (18–19), 2696–2707.
- Stavretis, S. E.; Atanasov, M.; Podlesnyak, A. A.; Hunter, S. C.; Neese, F.; Xue, Z.-L. Magnetic Transitions in Iron Porphyrin Halides by Inelastic Neutron Scattering and Ab Initio Studies of Zero-Field Splittings. *Inorg. Chem.* **2015**, *54* (20), 9790–9801.
- Neese, F.; Solomon, E. I. Calculation of Zero-Field Splittings, g-Values, and the Relativistic Nephelauxetic Effect in Transition Metal Complexes. Application to High-Spin Ferric Complexes. *Inorg. Chem.* **1998**, *37* (26), 6568–6582.
- Neese, F. Calculation of the zero-field splitting tensor on the basis of hybrid density functional and Hartree-Fock theory. *J. Chem. Phys.* **2007**, *127* (16), 164112.
- Okamoto, T.; Takahashi, H.; Ohmichi, E.; Ohta, H. Force-detected ESR Measurements in a Terahertz Range up to 0.5 THz and Application to Hemin. *Appl. Magn. Reson.* **2017**, *48* (5), 435–444.
- Okamoto, T.; Ohmichi, E.; Okubo, S.; Ohta, H. Precise Determination of Zero-Field Splitting Parameters of Hemin by High-Field and High-Frequency Electron Paramagnetic Resonance. *J. Phys. Soc. Jpn.* **2018**, *87* (1), 013702.
- Nehrkorn, J.; Telsler, J.; Hollmack, K.; Stoll, S.; Schnegg, A. Simulating Frequency-Domain Electron Paramagnetic Resonance: Bridging the Gap between Experiment and Magnetic Parameters for High-Spin Transition-Metal Ion Complexes. *J. Phys. Chem. B* **2015**, *119* (43), 13816–13824.
- Champion, P. M.; Sievers, A. J. Far infrared magnetic resonance in FeSiF<sub>6</sub>·6H<sub>2</sub>O and Fe(SPh)<sub>4</sub>·2-. *J. Chem. Phys.* **1977**, *66* (5), 1819–1825.
- Brackett, G. C.; Richards, P. L.; Wickman, H. H. Far infrared spectra of several Fe(III) complexes with spin S = 3/2. *Chem. Phys. Lett.* **1970**, *6* (2), 75–78.
- Brackett, G. C.; Richards, P. L.; Caughey, W. S. Far-Infrared Magnetic Resonance in Fe(III) and Mn(III) Porphyrins, Myoglobin, Hemoglobin, Ferrichrome A, and Fe(III) Dithiocarbamates. *J. Chem. Phys.* **1971**, *54* (10), 4383–4401.
- Champion, P. M.; Sievers, A. J. Far infrared magnetic resonance of deoxyhemoglobin and deoxymyoglobin. *J. Chem. Phys.* **1980**, *72* (3), 1569–1582.
- Dolphin, D. H.; Sams, J. R.; Tsin, T. B.; Wong, K. L. Moessbauer-Zeeman spectra of some octaethylporphyrinato- and tetraphenylporphyrinatoiron(III) complexes. *J. Am. Chem. Soc.* **1978**, *100* (6), 1711–1718.
- Hunter, S. C.; Podlesnyak, A. A.; Xue, Z.-L. Magnetic Excitations in Metalloporphyrins by Inelastic Neutron Scattering:

- Determination of Zero-Field Splittings in Iron, Manganese, and Chromium Complexes. *Inorg. Chem.* **2014**, *53* (4), 1955–1961.
- (30) Nishio, T.; Yokoyama, S.; Sato, K.; Shiomi, D.; Ichimura, A. S.; Lin, W. C.; Dolphin, D.; McDowell, C. A.; Takui, T. Ground-state high-spin iron (III) octaethylporphyrin as studied by single-crystal cw/pulsed ESR spectroscopy. *Synth. Met.* **2001**, *121* (1), 1820–1821.
- (31) Heinrich, B. W.; Braun, L.; Pascual, J. I.; Franke, K. J. Protection of excited spin states by a superconducting energy gap. *Nat. Phys.* **2013**, *9* (12), 765–768.
- (32) Krzystek, J.; Ozarowski, A.; Telsler, J. Multi-frequency, high-field EPR as a powerful tool to accurately determine zero-field splitting in high-spin transition metal coordination complexes. *Coord. Chem. Rev.* **2006**, *250* (17), 2308–2324.
- (33) Schnegg, A.; Behrends, J.; Lips, K.; Bittl, R.; Holldack, K. Frequency domain Fourier transform THz-EPR on single molecule magnets using coherent synchrotron radiation. *Phys. Chem. Chem. Phys.* **2009**, *11* (31), 6820–6825.
- (34) Hoffman, B. M. Electron-nuclear double resonance spectroscopy (and electron spin-echo envelope modulation spectroscopy) in bioinorganic chemistry. *Proc. Natl. Acad. Sci. U. S. A.* **2003**, *100* (7), 3575–3578.
- (35) Hoffman, B. M. ENDOR of Metalloenzymes. *Acc. Chem. Res.* **2003**, *36* (7), 522–529.
- (36) Lubitz, W.; Reijerse, E.; van Gestel, M. [NiFe] and [FeFe] Hydrogenases Studied by Advanced Magnetic Resonance Techniques. *Chem. Rev.* **2007**, *107* (10), 4331–4365.
- (37) Cox, N.; Retegan, M.; Neese, F.; Pantazis, D. A.; Bousiac, A.; Lubitz, W. Electronic structure of the oxygen-evolving complex in photosystem II prior to O-O bond formation. *Science* **2014**, *345* (6198), 804.
- (38) Ingram, D. J. E.; Gibson, J. F.; Perutz, M. F. Electron Spin Resonance in Myoglobin and Haemoglobin: Orientation of the Four Haem Groups in Haemoglobin. *Nature* **1956**, *178* (4539), 906–908.
- (39) Ingram, D. J. E.; Kendrew, J. C. Electron Spin Resonance in Myoglobin and Haemoglobin: Orientation of the Haem Group in Myoglobin and its Relation to the Polypeptide Chain Direction. *Nature* **1956**, *178* (4539), 905–906.
- (40) Pilbrow, J. R. *Transition Ion Electron Paramagnetic Resonance*; Clarendon Press, 1990.
- (41) Nehrkorn, J.; Holldack, K.; Bittl, R.; Schnegg, A. Recent progress in synchrotron-based frequency-domain Fourier-transform THz-EPR. *J. Magn. Reson.* **2017**, *280*, 10–19.
- (42) Helmholtz-Zentrum Berlin für Materialien und Energie; Holldack, K.; Schnegg, A. THz Electron Paramagnetic Resonance/THz Spectroscopy at BESSY II. *Journal of large-scale research facilities* **2016**, *2*, A51.
- (43) Scheidt, W. R.; Finnegan, M. G. Structure of monoclinic chloro(meso-tetraphenylporphyrinato)iron(III). *Acta Crystallogr., Sect. C: Cryst. Struct. Commun.* **1989**, *45* (8), 1214–1216.
- (44) Song, B.; Park, K.; Yu, B. Molecular Structure of 5,10,15,20-Tetrakis(pentafluorophenyl)Porphinatoiron(III) Chloride and F-19 NMR Investigation of Its Derivatives. *J. Korean Chem. Soc.* **1997**, *41* (9), 495–501.
- (45) Song, B.; Swenson, D. C.; Goff, H. M. Chloro[5,10,15,20-tetrakis(pentafluorophenyl)porphinato]iron(III) 0.57-Toluene Solvate. *Acta Crystallographica Section C* **1998**, *54* (11), No. IUC9800058.
- (46) Anzai, K.; Hatano, K.; Lee, Y. J.; Scheidt, W. R. Preparation and molecular stereochemistry of fluoro(meso-tetraphenylporphinato)iron(III). *Inorg. Chem.* **1981**, *20* (7), 2337–2339.
- (47) Skelton, B. W.; White, A. H. Crystal structure of Bromo-(tetraphenylporphyrin)iron(III). *Aust. J. Chem.* **1977**, *30* (12), 2655–2660.
- (48) Hatano, K.; Scheidt, W. R. Molecular stereochemistry of iodo(meso-tetraphenylporphinato)iron(III). *Inorg. Chem.* **1979**, *18* (3), 877–879.
- (49) Heinrich, B. W.; Braun, L.; Pascual, J. I.; Franke, K. J. Tuning the Magnetic Anisotropy of Single Molecules. *Nano Lett.* **2015**, *15* (6), 4024–4028.
- (50) Koenig, D. The structure of [alpha]-chlorohemin. *Acta Crystallogr.* **1965**, *18* (4), 663–673.
- (51) Senge, M. Chloro(2,3,7,8,12,13,17,18-octaethylporphyrinato)-iron(III). *Acta Crystallogr., Sect. E: Struct. Rep. Online* **2005**, *61* (2), m399–m400.
- (52) Kohnhorst, S. A.; Haller, K. J. Chlorido(2,3,7,8,12,13,17,18-octaethylporphyrinato)iron(III): a new triclinic polymorph of Fe(OEP)Cl. *Acta Crystallogr., Sect. C: Struct. Chem.* **2014**, *70* (4), 368–374.
- (53) Sahoo, D.; Quesne, M. G.; de Visser, S. P.; Rath, S. P. Hydrogen-Bonding Interactions Trigger a Spin-Flip in Iron(III) Porphyrin Complexes. *Angew. Chem., Int. Ed.* **2015**, *54* (16), 4796–4800.
- (54) Hassan, A. K.; Pardi, L. A.; Krzystek, J.; Sienkiewicz, A.; Goy, P.; Rohrer, M.; Brunel, L. C. Ultrawide Band Multifrequency High-Field EMR Technique: A Methodology for Increasing Spectroscopic Information. *J. Magn. Reson.* **2000**, *142* (2), 300–312.
- (55) Stoll, S.; Schweiger, A. EasySpin, a comprehensive software package for spectral simulation and analysis in EPR. *J. Magn. Reson.* **2006**, *178* (1), 42–55.
- (56) Nehrkorn, J.; Schnegg, A.; Holldack, K.; Stoll, S. General Magnetic Transition Dipole Moments for Electron Paramagnetic Resonance. *Phys. Rev. Lett.* **2015**, *114* (1), 010801.
- (57) Dogutan, D. K.; Bediako, D. K.; Teets, T. S.; Schwalbe, M.; Nocera, D. G. Efficient Synthesis of Hangman Porphyrins. *Org. Lett.* **2010**, *12* (5), 1036–1039.
- (58) Lindsey, J. S.; Wagner, R. W. Investigation of the synthesis of ortho-substituted tetraphenylporphyrins. *J. Org. Chem.* **1989**, *54* (4), 828–836.